Microstructural degradation of silicon electrodes during lithiation observed via *operando* X-ray tomographic imaging

CrossMark

Oluwadamilola O. Taiwo [a], Juan M. Paz-García [b], Stephen A. Hall [b], Thomas M.M. Heenan [a], Donal P. Finegan [a], Rajmund Mokso [c], Pablo Villanueva-Pérez [c], Alessandra Patera [c, d], Daniel J.L. Brett [a], Paul R. Shearing [a, *]

[a] *Electrochemical Innovation Lab, Department of Chemical Engineering, University College London, WC1E 7JE, UK*
[b] *Division of Solid Mechanics, Lund University, Lund, Sweden*
[c] *Swiss Light Source, Paul Scherrer Institut, CH-5232 Villigen, Switzerland*
[d] *Centre d'Imagerie BioMedicale, Ecole Polytechnique Federale de Lausanne, 1015 Lausanne, Switzerland*

HIGHLIGHTS

- Si particle evolution in early stage of lithiation was captured using X-ray CT.
- Fracturing of Si particles during incremental lithiation was visualised.
- Lithiation-induced micro-cracks propagate within particles leading to fracturing.
- Si particle lithiation as a function of distance from current collector was studied.

ARTICLE INFO

ABSTRACT

Due to their high theoretical capacity compared to that of state-of-the-art graphite-based electrodes, silicon electrodes have gained much research focus for use in the development of next generation lithium-ion batteries. However, a major drawback of silicon as an electrode material is that it suffers from particle fracturing due to huge volume expansion during electrochemical cycling, thus limiting commercialization of such electrodes. Understanding the role of material microstructure in electrode degradation will be instrumental in the design of stable silicon electrodes. Here, we demonstrate the application of synchrotron-based X-ray tomographic microscopy to capture and track microstructural evolution, phase transformation and fracturing within a silicon-based electrode during electrochemical lithiation.

© 2016 The Authors. Published by Elsevier B.V. This is an open access article under the CC BY license (http://creativecommons.org/licenses/by/4.0/).

1. Introduction

Lithium-ion batteries are ubiquitous as power sources in portable electronic devices due to their high energy density and long cycle life, and are now being extended to applications such as electric vehicles and grid energy storage [1,2]. To meet such demanding electronic applications, the development of high-performance lithium-ion batteries is crucial and significant research effort has been devoted to achieve this. Carbonaceous materials such as graphite are commonly used as negative electrodes in traditional lithium-ion batteries; these materials have high Coulombic efficiencies (>90%) but are limited by their rather low specific capacities (372 mAhg^{-1}). Materials that form alloys with lithium (e.g. Sn, Sb, Si, and Ge) [3] are being considered as replacements for graphite due to their much higher theoretical specific capacities.

Amongst alloy-type electrode materials, silicon (Si) is a particularly promising candidate studied because its reaction with lithium occurs at low discharge potentials (<0.5 V vs. Li/Li$^+$) [4], and it possesses a large theoretical specific capacity (ca. 4200 mAhg^{-1}, [5]). However, a major challenge of the application of silicon in rechargeable lithium batteries is the huge volume expansion of silicon (up to 300% [6]) upon lithiation, leading to material

fracturing and pulverization, which results in loss of electrical contact and rapid capacity fading within the battery.

Numerous strategies have been proposed to mitigate these failure mechanisms in Si electrodes; for example: nanostructured Si materials, such as nanowires [7–10] and carbon-coated nano-composites [11–14]; conductive and self-healing polymer binders [15,16]; modified cycling protocols [6]. Although nano-sized Si materials have been shown to mitigate the severe fracturing associated with lithiation-induced volume expansion, their high production cost, poor first- and later-cycle Coulombic efficiency, and significant solid electrolyte interphase (SEI) formation still remain major drawbacks to their use in commercial battery

applications. Therefore, the use of low cost, more readily available Si microparticles (SiMPs) as electrode materials appears promising. However, a clear understanding of the degradation and failure of SiMPs during battery operation is crucial.

Visualization of morphological changes that occur in Si, as well as other alloying-type electrode materials, during electrochemical cycling have previously been carried out *in situ* using two-dimensional (2D) imaging techniques; for example, using *in situ* transmission electron microscopy [17–20], and *in situ* atomic force microscopy [21–23]. However, recent advances in tomography techniques have provided unprecedented insight into the micro-structural evolution in Li-ion battery electrode materials in three-
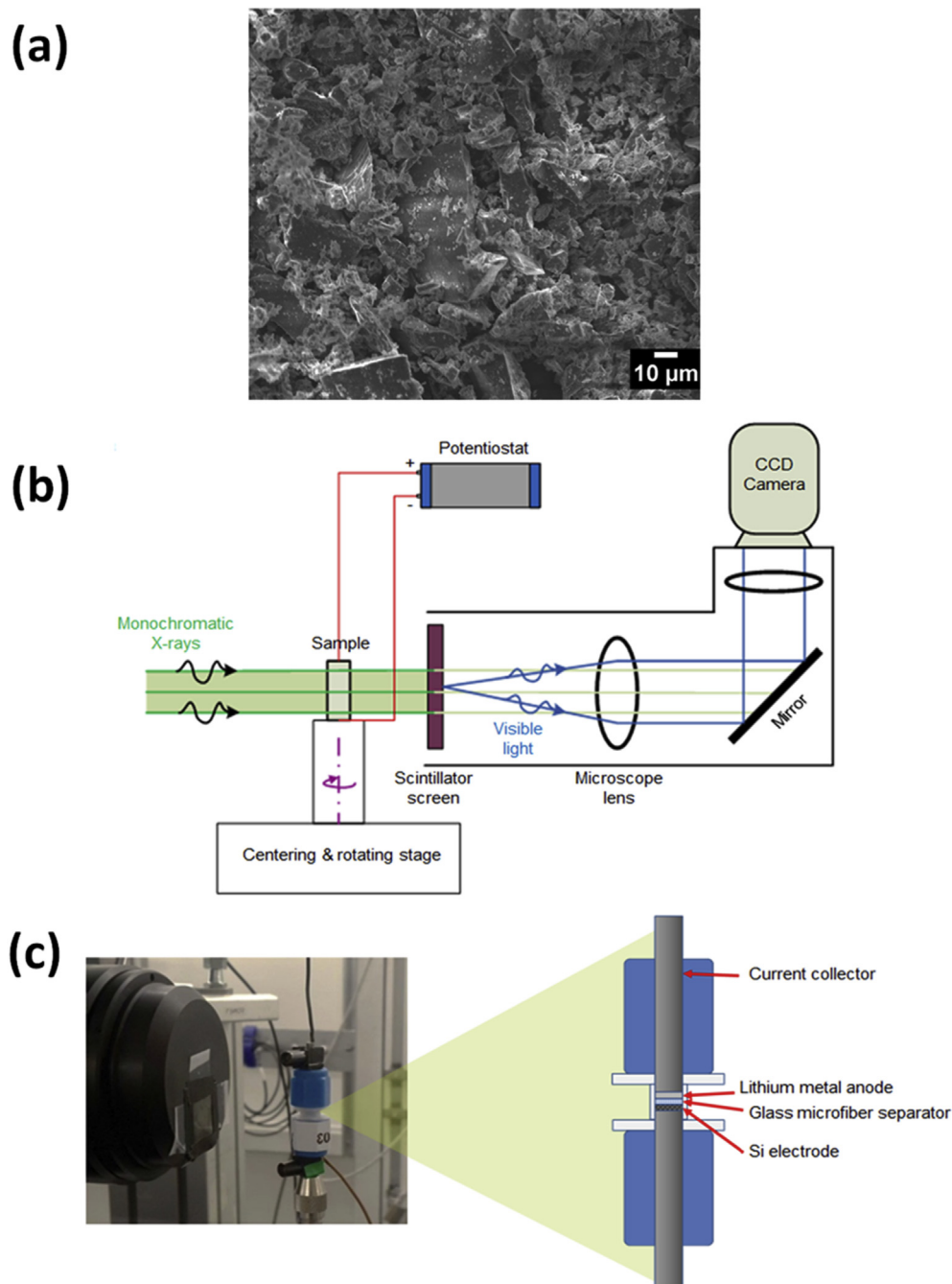
Fig. 1. (a) Scanning electron micrograph of the micron-sized Si particles. (b) Schematic illustration of the experimental setup at the TOMCAT beamline. (c) Assembled battery cell made from PFA Swagelok tube fitting and designed to enable operando X-ray CT.

dimensions. Amongst these techniques, X-ray computed tomography (CT), using both laboratory and synchrotron X-ray sources, has proven to be a powerful, non-invasive diagnostic tool that provides a platform for *in situ* and *operando* examination of temporal changes in electrode materials resulting from battery operation or failure [24–29]. Recently, Gonzalez et al. [30] and Paz-Garcia et al. [31] performed *in situ* visualization of microstructural evolution in Si-based electrodes using laboratory X-ray micro-CT at different stages of electrode lithiation. In these studies, volume expansion and phase transformation could be analysed at electrode and particle levels. The higher X-ray flux achievable with synchrotron X-ray sources [32] leads to significantly faster image acquisition times, enabling higher spatial and temporal resolution imaging. Therefore, synchrotron CT enables dynamic morphological
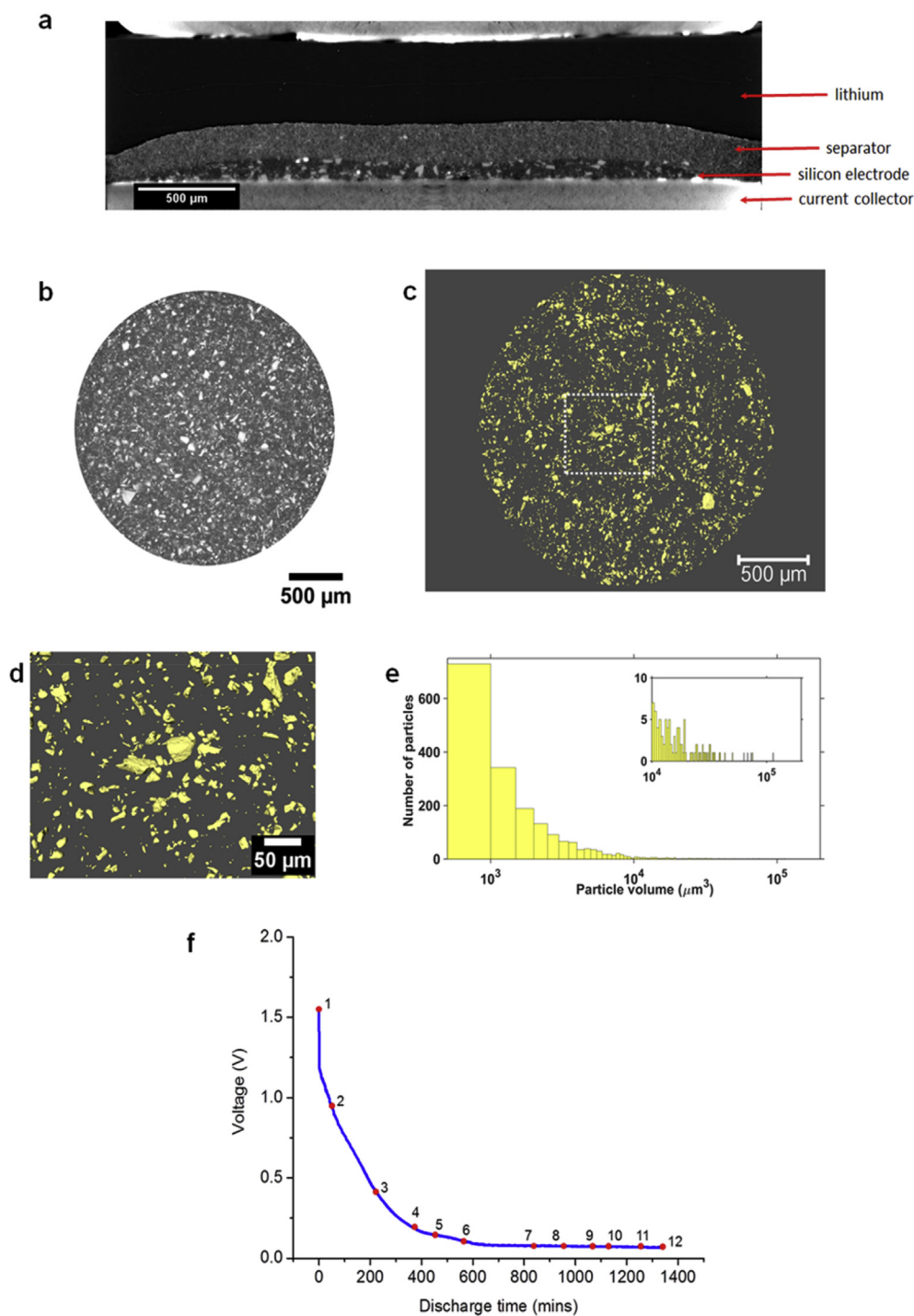
Fig. 2. (a) Vertical cross-section through X-ray tomogram showing the entire cell assembly. (b) Transverse cross-section through the X-ray tomogram, showing the Si composite electrode. (c) 3D rendering of the thresholded tomogram showing dense Si particles within the composite electrode before cell discharge. (d) Zoomed-in image of rendered particles shows their non-uniform shape distribution. (e) Si particle volume distribution within the entire electrode before cell discharge. Inset in (e): volumetric distribution at volumes greater than 1×10^4 μm^3. (f) Galvanostatic discharge profile of the Si/Li half-cell at a constant rate of 50 mAg^{-1}. 12 of the 72 tomographic scans taken at different stages during discharge (marked in red dots) are selected for subsequent analysis. (For interpretation of the references to colour in this figure legend, the reader is referred to the web version of this article.)

evolution and degradation of materials to be captured in real time; for instance, during continuous battery operation.

In this work, we capture the microstructural dynamics and degradation mechanisms associated the lithiation of SiMPs in 3D using *operando* synchrotron-based X-ray tomographic microscopy. With the aid of a custom-built X-ray transparent cell, we are able to track lithiation-induced structural changes within the entire cell assembly, as well as the morphological evolution and phase transformations within individual SiMPs during electrochemical testing.

2. Methods

### 2.1. Electrode preparation and cell fabrication

For the electrode slurry preparation, micron-sized Si powder (<300 mesh, 99% purity), conductive carbon and polyvinylidene fluoride (PVDF) in respective weight ratios 3:6:1 were mixed with *N*-methylpyrrolidone (NMP) in a ULTRA-TURRAX IKA® homogenizer. A scanning electron micrograph of the micro-sized Si particles is shown in Fig. 1a. All chemicals used in the electrode slurry preparation step were procured from Pi-Kem Ltd., UK. After mixing, the resulting slurry was then coated onto the tip of steel current collecting pins (ca. 3.2 mm in diameter). Slurry-coated pins were placed in a vacuum oven at 80 °C to dry for 12 h. The mass of Si within the dried electrode was estimated by weighing the current collecting pins before and after slurry coating.

Half-cells were then assembled within custom-built thin-walled X-ray transparent PFA Swagelok cell housings [25] in an argon-filled glove-box (oxygen and moisture levels in the glove-box were maintained at < 0.5 ppm) with a metallic lithium foil counter electrode (Pi-Kem Ltd.), a borosilicate glass fibre separator (Whatmann GF-D grade, GE), and electrolyte containing 1M $LiPF_6$ in mixture of ethylene carbonate (EC): ethyl methyl carbonate (EMC) in the ratio 3:7 by volume.

2.2. Operando X-ray tomographic imaging

Synchrotron-based X-ray tomographic studies of the lithiation dynamics within silicon-based electrodes were performed at the TOMCAT beamline of the Swiss Light Source (Paul Scherrer Institut, Villigen, Switzerland) which enables fast, non-invasive imaging at sub-micron resolution [33]. The experimental setup for the tomographic imaging is shown in Fig. 1b. An assembled Si–Li half-cell was mounted on the sample stage as shown in Fig. 1c to enable galvanostatic cell discharge whilst simultaneously acquiring tomographic images. The cell was imaged in a 17 keV parallel monochromatic X-ray beam with a field-of-view (FOV) of 1.6 mm × 1.4 mm, corresponding to half the size of the cell assembly: the sample stage rotation axis was positioned at the edge of the FOV, such that it was possible to capture the entire cell assembly by a full 360° rotation. 3001 projection images were acquired during the rotation of the sample about its long axis, through angular steps of 0.12° with an exposure time of 110 ms for each projection image. The transmitted X-rays illuminated a 20 μm thick LuAG:Ce scintillator (Crytur Ltd., Turnov, Czech Republic), producing visible light which was focused onto a PCO. Edge camera with a high-speed CMOS detector. A total scan time of 5.5 min per tomogram was achieved with an effective voxel size of 650 nm − a significant improvement in both temporal and spatial resolution to previous laboratory-based X-ray tomography studies on Si electrodes [30].

Galvanostatic cell discharge was performed using a potentiostat (Ivium CompactStat, Ivium Technologies). Tomograms of the entire electrode were acquired every 18 min during galvanostatic discharge at a rate of 50 mAg^{-1}. At this discharge rate, the lithiation kinetics, and thus microstructural dynamics of Si, was slow enough to be effectively captured in successive tomograms, and negligible material displacement was observed at the employed imaging frequency.
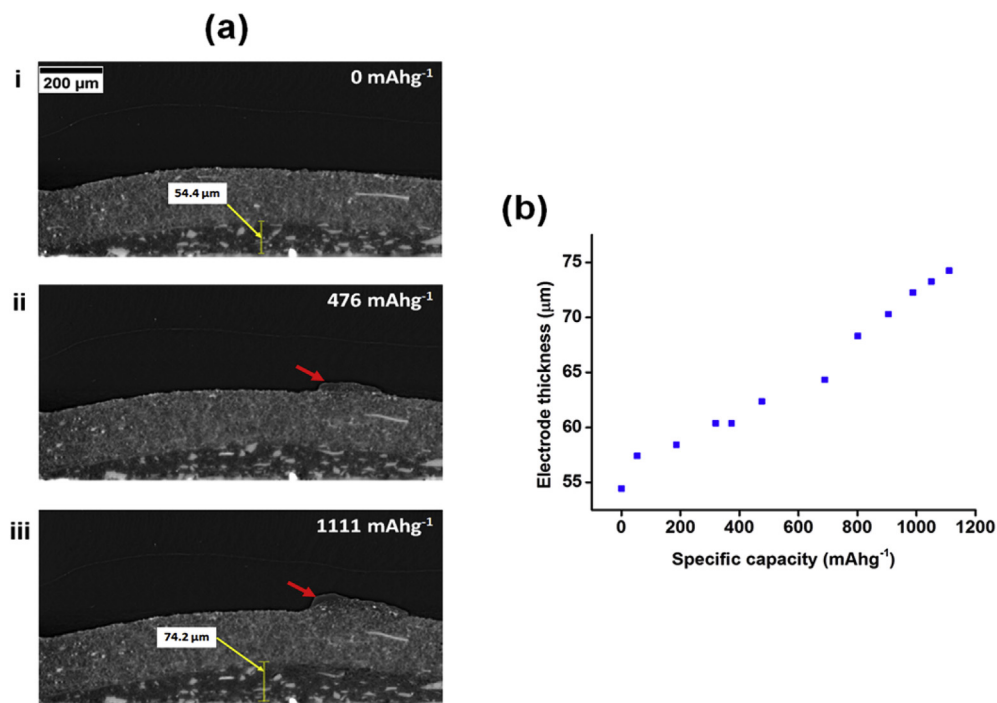

Fig. 3. . (a) 2D section through reconstructed tomogram of a region of the cell assembly showing increase in the silicon electrode thickness and the growth of surface pitting (highlighted by the red arrows) in the lithium counter electrode. Yellow lines in (i) and (iii) highlight the electrode thicknesses. (b) Change in electrode thickness with specific capacity during the lithiation process. (For interpretation of the references to colour in this figure legend, the reader is referred to the web version of this article.)

2.3. Image data processing

Each projection image collected during the tomography scans was corrected with the respective dark and flat-field image. Single-image phase and intensity extraction was also applied to all projection images with the aid of the Paganin phase-retrieval algorithm [34]; 3D reconstruction of the data was achieved using the gridrec algorithm [35].

To ease image analysis and computation of the resulting large image stacks, whilst maintaining significant image feature quality, the reconstructed images were converted from 16-bit to 8-bit TIFF

format. 3D visualization of reconstructed tomograms were processed using Avizo 9.0 (FEI Visualization Group, France) and ImageJ [36]. The dense Si particles were separated from the electrode conductive matrix and electrolyte/pore phase based on their difference in greyscale value via threshold segmentation in the Avizo segmentation editor. Particle volume distribution measurements were obtained by performing 3D connected component analysis of the segmented Si particles. Volume specific surface area calculations were performed in Avizo, and were based on a marching cubes algorithm [37] with surface mesh smoothing and refinement. The mean greyscale intensity within the cropped regions of
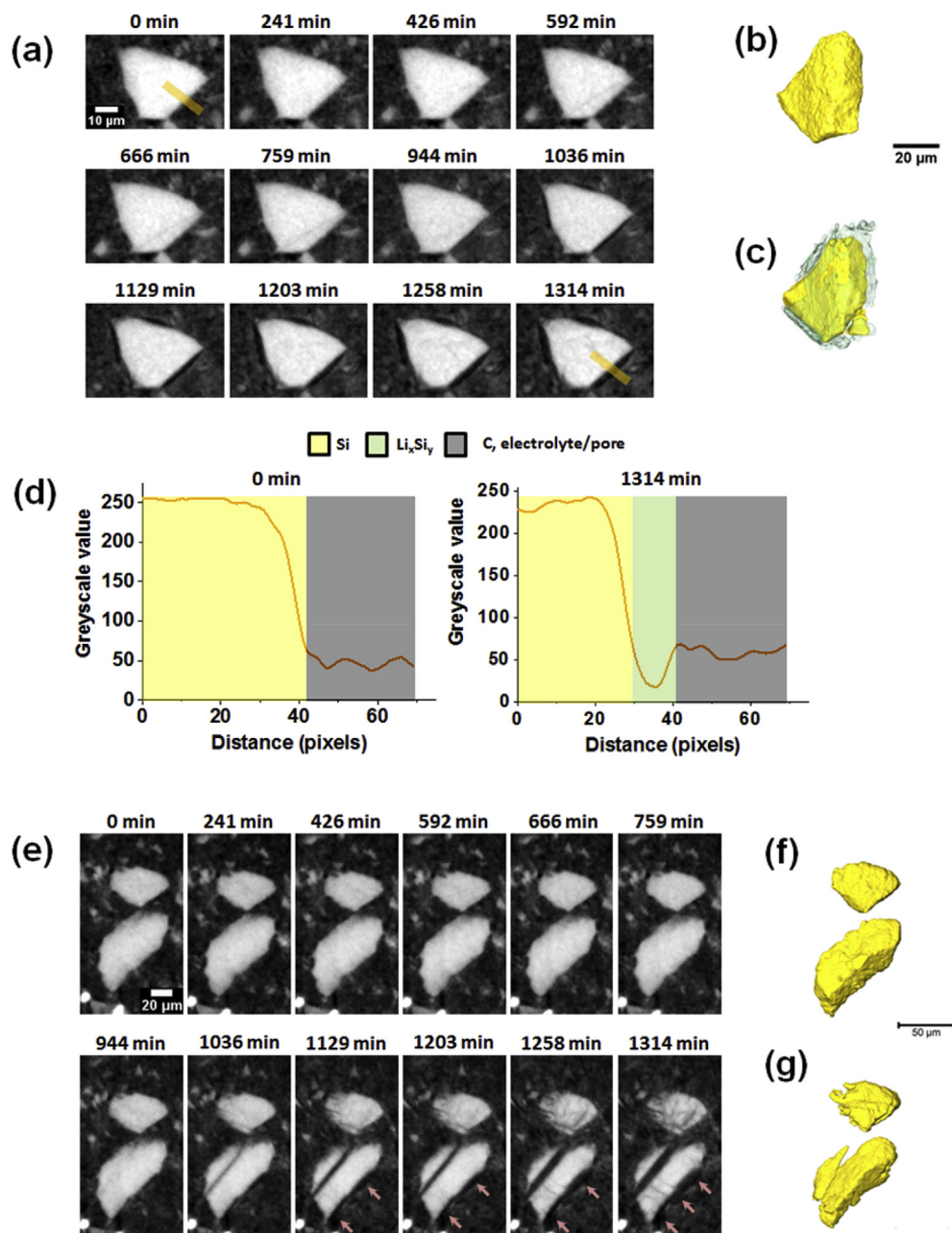
Fig. 4. X-ray tomogram sections of selected SiMPs showing varying initial responses on Si particles to lithiation-induced stresses. The particle in (a) gradually lithiates, with the formation of a low attenuating Li_xSi_y phase on the particle surface which grows inward. (b.c) 3D renderings of the particle in (a) at 0 min and 1314 min respectively. The histograms in (d) are the result of an intensity line scan [orange line in tomogram section at 0 min and 1314 min in (a)] showing the phase transformation at the particle boundary. The yellow, green and grey sections in the histograms highlight the crystalline Si, Li_xSi_y and surrounding carbon phases respectively. The two adjacent particles in (e) respond differently to lithiation stresses: both particles experience micro-cracking which eventually leads to the formation of complex crack microstructure in the top particle and fracturing in the bottom particle. Pink arrows highlight the gradual formation of the low attenuating Li_xSi_y phase. (f,g) 3D renderings of the particle in (e) at 0 min and 1314 min respectively. (For interpretation of the references to colour in this figure legend, the reader is referred to the web version of this article.)

interests containing particles was calculated by summing and averaging the greyscale values of the voxels in the selected region.

3. Results and discussion

With the synchrotron X-ray imaging setup, 72 tomogram datasets were acquired during a galvanostatic discharge of the cell (Fig. 2f). In the course of the galvanostatic cell discharge (*ca.* 22 h), the entire electrode undergoes partial lithiation (*ca.* 30% lithiation), reaching a specific discharge capacity of 1094 mAhg^{-1} out of an achievable 3579 mAhg^{-1} for the given electrode material.

Vertical and horizontal cross-sections through an X-ray tomogram of the half-cell assembly are presented in Fig. 2a; the horizontal section intersects the cell at the level of the Si electrode. The dense Si particles can be differentiated from the conductive matrix and electrolyte/pore phases by their higher X-ray attenuation. The Si particles can thus be isolated via threshold segmentation before rendering in 3D (Fig. 2c−d). On close inspection of the electrode volume rendering (Fig. 2d), the non-uniform shape distribution of the SiMPs can be seen.

Fig. 2e shows the volume distribution of SiMPs within the electrode prior to any electrochemical reduction, with particle count plotted against particle volume (*x* axis is plotted with logarithmic scale). The electrode sample shows a high frequency of small sized SiMPs and measured particle volumes ranged between 6.60 μm^3 and 11 × 10^4 μm^3. Assuming spherical shaped particles, these volumes would correspond to equivalent minimum and maximum particle diameters of 2.33 μm and 60.1 μm, and a mean particle diameter of 11.7 μm.

To track changes within the half-cell assembly, 12 of the 72 tomograms acquired during discharge were selected (Fig. 2f). Fig. 3a shows that the lithiation process induced volume expansion of the Si particles and the conductive matrix which led to a gradual increase in the thickness of the entire electrode. Fig. 3b shows the evolution of the electrode, which appears to increase from 54.4 μm to 74.2 μm after 30% lithiation.

Whilst the Si electrode increases in thickness, the lithium metal electrode surface exposed to electrolyte undergoes oxidation into Li$^+$ ions. Previous experimental work has shown that, at low current densities, this often results in electrochemical pitting of the lithium metal surface [38]. Such phenomenon is observed here and is marked by red arrows in Fig. 3a.

The formation of these pits can be attributed to the breakdown of the passive film layer on the surface of the lithium metal, which could be induced by the diffusion of hexafluorophosphate (PF$_6^-$) ions through the film [38]. The pit formation is also captured in the time lapse movies made from radiography images and the reconstructed image slices (Videos S1 and S2 respectively).

Supplementary videos related to this article can be found at http://dx.doi.org/10.1016/j.jpowsour.2016.12.070.

During cell discharge, the irregular shaped SiMPs in the electrode sample showed varying initial microstructural responses, such as phase transformation and fracturing, to lithiation-induced stresses. These varying structural responses were identified by selecting some of the largest SiMPs within the composite electrode and tracking their temporal evolution during the lithiation process. From here on, the tomograms are referred to by time-stamps as referenced to the electrochemical cycling data in Fig. 2f.

Between 1036 min and 1314 min, the X-ray tomogram sections of the particle in Fig. 4a show an uneven, inward growth of a low attenuating front. This low attenuating layer is associated with the formation of the low density Li$_x$Si$_y$ phase upon electrochemical lithiation of Si via a two-phase mechanism on the surface of the crystalline Si [39−41], forming a core-shell like structure. The non-uniform growth of the low attenuating Li$_x$Si$_y$ layer observed around the crystalline Si particle can be explained by a number of
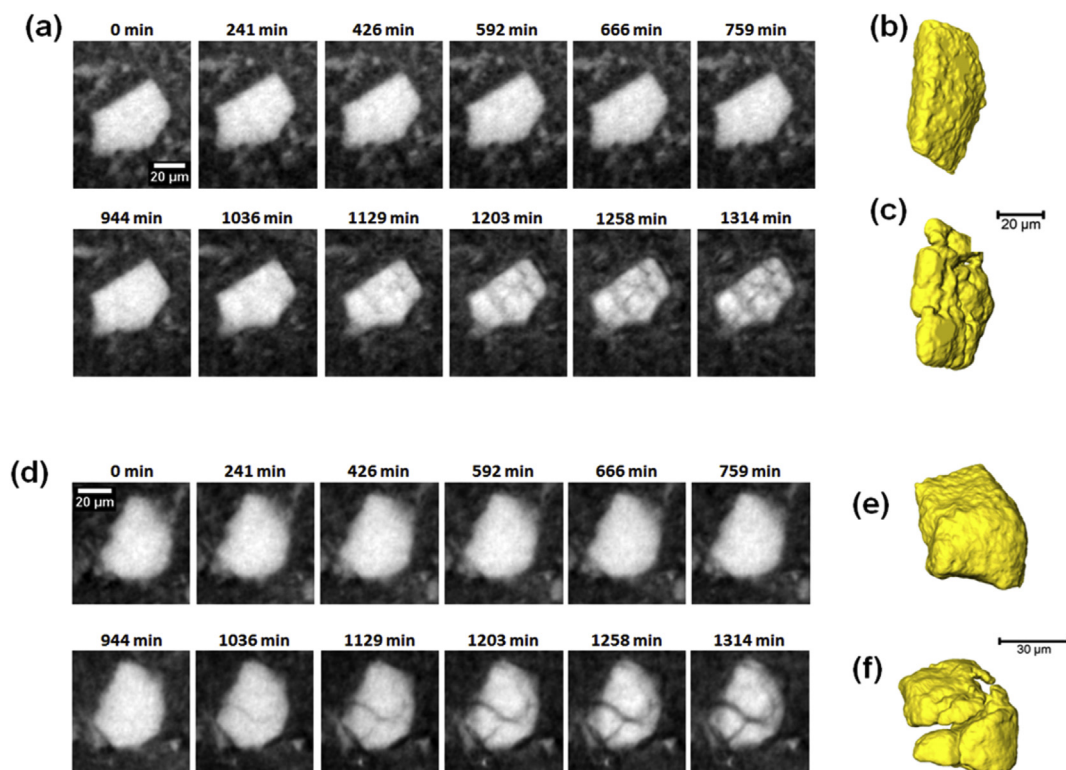
Fig. 5. Micro-crack initiation and propagation in SiMPs. X-ray tomogram cross sections show that micro-cracks could initially propagate within a SiMP to form a complex network of small cracks as in (a) or form longer and wider cracks as in (b). 3D renderings show the crystalline Si phase in particle (b,e) before lithiation and (c,f) after lithiation.
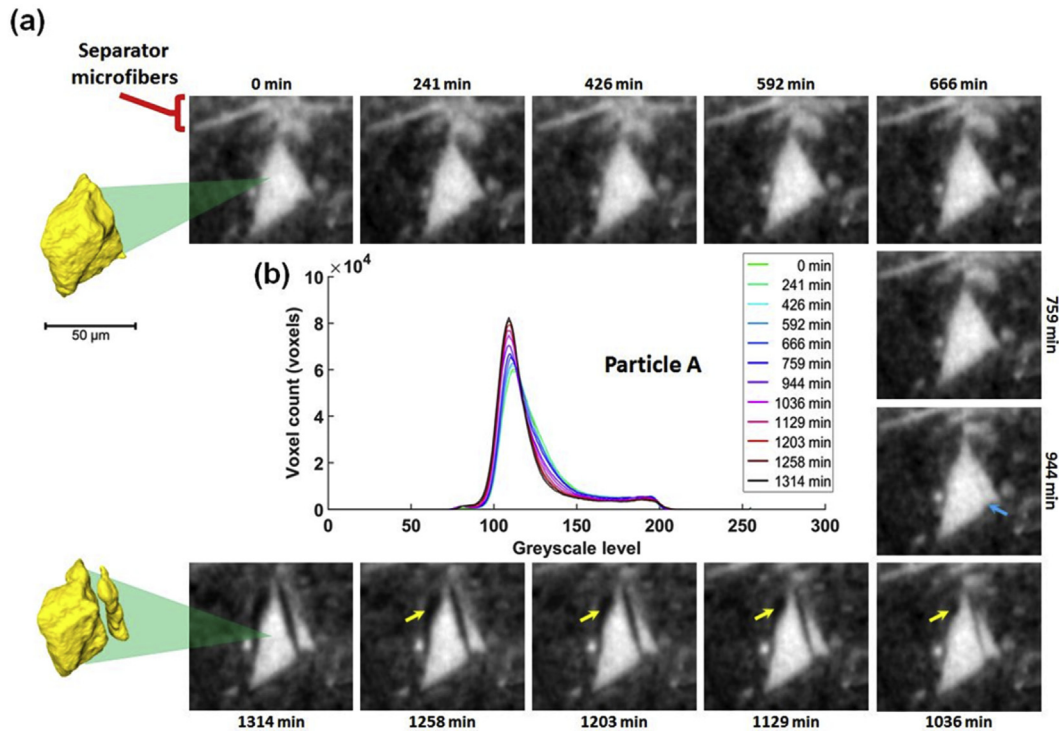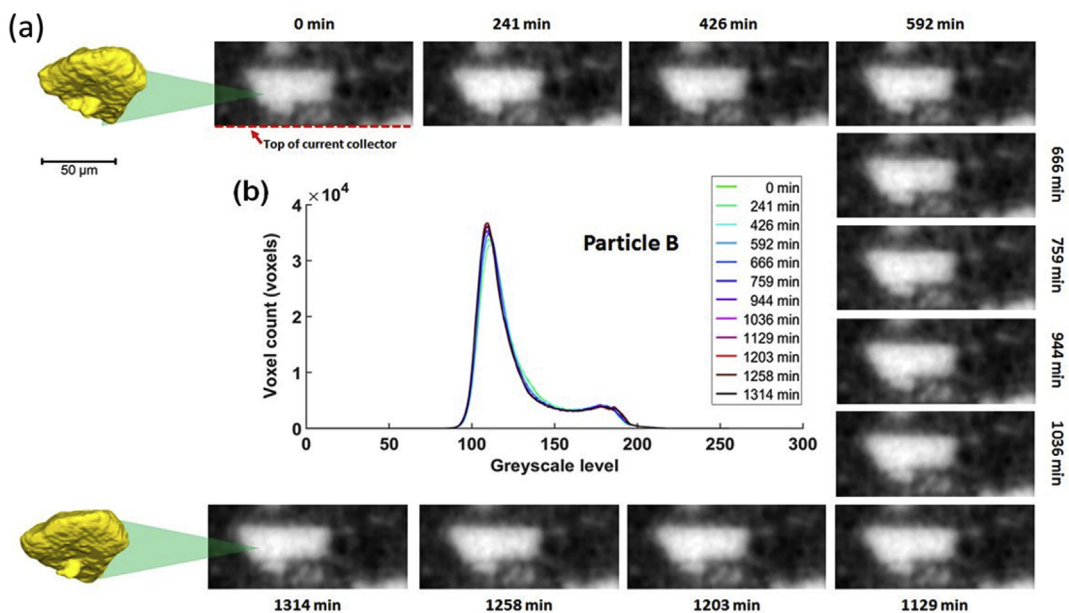
Fig. 6. (a) Evolution of Particle A during electrode lithiation. Particle A is located very close to the lithium source. (b) Evolution of the greyscale intensity histogram of the cropped region of interest containing Particle A during the lithiation process. Blue arrow indicates point of crack initiation, yellow arrows highlight gradual Si phase transformation at the particle boundary. (For interpretation of the references to colour in this figure legend, the reader is referred to the web version of this article.)

experimental and modelling studies that have shown that the growth of the lithiated silicon phase is anisotropic due to lithiation occurring preferentially in a particular crystal plane direction [42–45,47]. An intensity line scan performed across the crystalline Si, lithiated Si and the surrounding conducting matrix in the X-ray tomogram section at 1314 min (Fig. 4d) shows a significant difference in contrast between the highly absorbing crystalline Si phase and low absorbing lithiated Si layer, but with less contrast between

the lithiated phase and the surrounding conductive matrix. This makes threshold-based segmentation between both low density phases challenging.

In the tomogram captured at 1036 min (Fig. 4e), the formation of micro-cracks is observed in both particles. As lithiation progresses, a main crack in the lower particle propagates until particle fracture occurs. A complex vein-like network of micro-cracks forms in the top particle. In the lower particle, formation of the low attenuating

Fig. 7. (a) Evolution of Particle B during electrode lithiation. Particle B is located very close to the electrode current collector. (b) Evolution of the greyscale intensity histogram of the cropped region of interest containing Particle B showing little change during the lithiation process.

Li_xSi_y phase appears to take place preferentially on one surface parallel to the main crack, as indicated by the pink arrows in the tomograms in Fig. 4e. Choi et al. [48] observed that the nature of micro-crack generation and propagation to form complete fractures in crystalline Si was dependent on the crystal orientation. Using TEM, they revealed the formation of micro-cracks in crystalline Si upon initial lithiation, which subsequently contributed to the formation of a complex vein-like network of Li_xSi_y within the crystalline Si matrix, proposing that these micro-cracks act as fast diffusion paths for lithium, and generate a network of interconnecting cracks within the crystalline Si. Fig. 5 shows how different morphologies of micro-cracks form within two further SiMPs over the same lithiation period. At 1314 min, a more complex network of small multiple cracks is seen in the SiMP in Fig. 5a, while longer and wider cracks are seen in the particle in Fig. 5d.

It is noteworthy to mention that the varied structural responses observed amongst the highlighted individual SiMPs could be due to any of (or a combination of) the following factors: anisotropic kinetics of the lithiation process at the Si/Li_xSi_y interface, presence of manufacture-induced surface defects prior to electrochemical reduction, formation of lithiation-induced defects that provide faster Li^+ diffusion pathways, quality of electrical contact between active particles and the conducting phase.

At the imaging resolution employed, no size-dependent fracturing was observed amongst the SiMPs within the electrode upon lithiation. However, higher resolution *in situ* TEM imaging studies have shown that there exists a critical particle size above which fracturing occurs during lithiation and delithiation, and it is typically ~150 nm in Si nanoparticles [46] and ~250 nm in Si nanowires [49]. However, a number of large SiMPs in this study were observed to not display severe fracturing over the course of the lithiation process; the particle captured in Fig. 4a is a typical example.

The extent of particle lithiation as a function of distance from electrode current collector was also examined. Overall, it was observed that Si particles closest to the electrode-separator interface experienced the most morphological change upon lithiation of the electrode, whereas particles furthest from the separator showed little or no transformation during the cell discharge. Figs. 6 and 7 and show two large particles selected from the centre region of the electrode layer tracked over the lithiation process; one from the top of the composite electrode, close to the separator (Particle A) and the other from close to the Si electrode current collector (Particle B). The morphological evolution of Si phase in the two SiMPs upon lithiation is shown in 3D as a time-lapse movie in Video S3 (See Supplementary Information).

Supplementary video related to this article can be found at http://dx.doi.org/10.1016/j.jpowsour.2016.12.070.

Compared to Particle A (Fig. 6), Particle B (Fig. 7) experienced minimal morphological and attenuation changes as a result of the lithiation process, which suggests that the particle lithiation within the electrode in this study is limited by Li^+ transport, and not by electronic conductivity. As the cell discharge progresses, Particle A gradually lithiates, with micro-crack formation seen at 994 min (marked by blue arrow in Fig. 6a). The crack then propagates up until complete particle fracture occurs, with the particle breaking down into smaller fragments. The fracture process could cause a loss of electrical contact between the active Si surface and the conductive matrix, and increase the crystalline Si surface area for additional SEI formation. Growth of the weakly attenuating Li_xSi_y phase appears to initiate locally (at 1036 min) and spread along the particle surface (marked by yellow arrows in Fig. 6a). The increase in magnitude of the greyscale intensity peak and the slight peak shift to even lower greyscale values seen in Fig. 6b can be associated with lithiation-induced phase transformation within and around the particle.

Changes in specific surface area and volume of the residual crystalline Si phase, and changes in mean greyscale intensity of the entire cropped region of interest containing both sampled particles were tracked as a function of electrode discharge capacity and are shown in Fig. 8. The sudden increase in volume-specific surface area of the dense Si phase in Particle A after 476 mAhg^{-1} can be associated with particle fracturing seen in Fig. 6 which leads
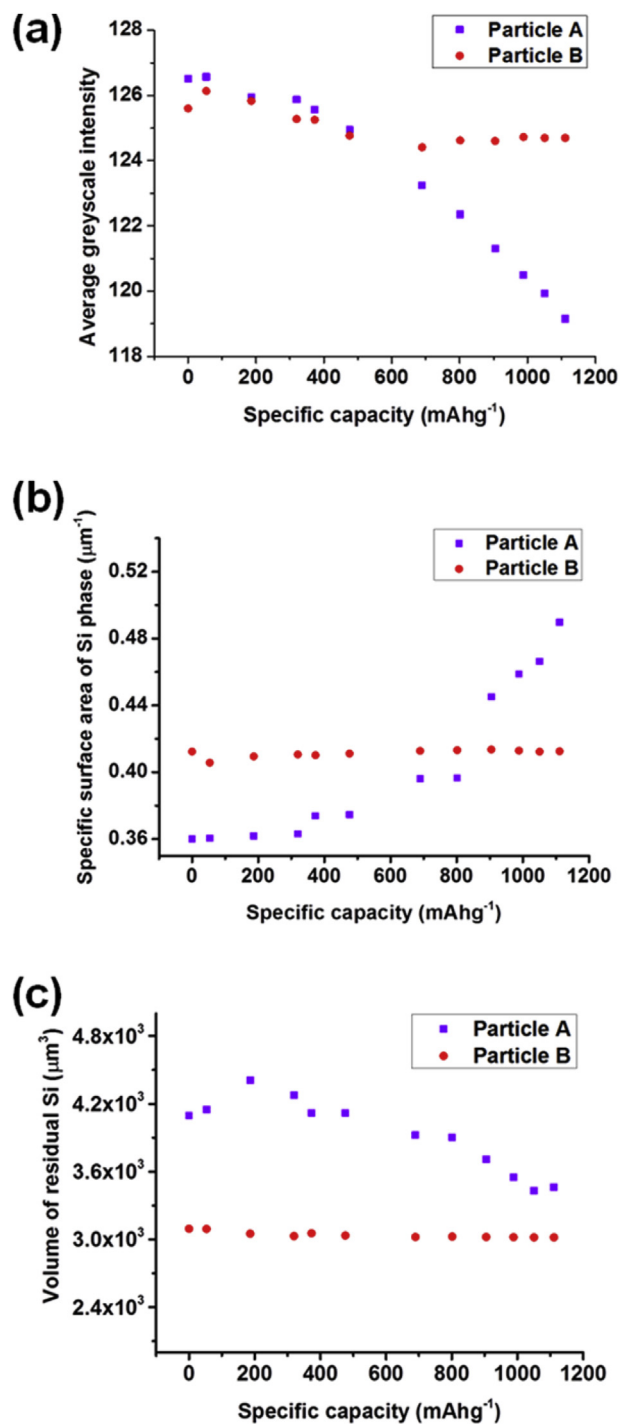

Fig. 8. (a) Change in average greyscale intensity of the cropped region of interest containing Particle A (further from the electrode current collector) and Particle B (closer to the electrode current collector). (b) Change in volume-specific surface area and (c) volume of residual crystalline Si phase for both particles as a function of electrode specific capacity.

increase in exposed Si surface. In addition to a reduction in the residual Si phase volume, a decrease in the mean greyscale intensity is seen to occur in the region of interest around Particle A. This also shows evidence of phase change within the conductive matrix surrounding the main particle as well as the occurrence particle crack formation.

4. Conclusions

In summary, synchrotron X-ray tomographic microscopy has been used to observe spatial and temporal morphological evolution within a composite silicon electrode during lithiation. *Operando* 3D X-ray imaging enabled visualization of fracture formation and propagation in individual SiMPs, difficult to achieve using laboratory X-ray sources. Surface pitting was captured upon electrochemical stripping of the lithium metal counter electrode.

Selected SiMPs showed varied structural responses to lithiation-induced stresses by surface growth of low-absorbing Li_xSi_y phase and developing micro-cracks which propagate and lead to particle fracture. Particles closest to the separator surface (or to the Li^+ source) undergo most lithiation and experience severe fracturing, indicating that the lithiation in the composite electrode under study is not limited by electronic conductivity, but by the diffusion of Li^+ ions through the electrode layer. In addition, these X-ray CT results highlight the severe nature of fracturing of crystalline SiMPs during the first lithiation, which often leads to commonly observed irreversible capacity loss in Si electrodes after the first charge-discharge cycle. Although this fracturing in SiMPs remains unavoidable, strategies to stabilize their performance and maintain their electrical conductivity are being developed, such as, for example, graphene encapsulation [50].

This study not only demonstrates that the dynamic morphological transformations that occur during the degradation and failure of SiMPs can be non-invasively studied in real time using synchrotron X-ray imaging, but that the technique is useful in providing valuable information and insight to aid efficient design of micron-sized silicon particles for electrodes in next generation batteries.

Acknowledgements

References

[1] M. Armand, J.-M. Tarascon, Nature 451 (2008) 652.
[2] B. Kang, G. Ceder, Nature 458 (2009) 190.
[3] D. Larcher, S. Beattie, M. Morcrette, K. Edström, J.-C. Jumas, J.-M. Tarascon, J. Mater. Chem. 17 (2007) 3759.
[4] H. Jung, J. Power Sources 115 (2003) 346.
[5] J.O. Besenhard, J. Yang, M. Winter, J. Power Sources 68 (1997) 87.
[6] M.N. Obrovac, L.J. Krause, J. Electrochem. Soc. 154 (2007) A103.
[7] C.K. Chan, H. Peng, G. Liu, K. McIlwrath, X.F. Zhang, R.A. Huggins, Y. Cui, Nat. Nanotechnol. 3 (2008) 31.
[8] K. Peng, J. Jie, W. Zhang, S.-T. Lee, Appl. Phys. Lett. 93 (2008), 033105(1−3).
[9] M. Ge, J. Rong, X. Fang, C. Zhou, Nano Lett. 12 (2012) 2318.
[10] L.-F. Cui, R. Ruffo, C.K. Chan, H. Peng, Y. Cui, Nano Lett. 9 (2009) 491.
[11] A. Magasinski, P. Dixon, B. Hertzberg, A. Kvit, J. Ayala, G. Yushin, Nat. Mater 9 (2010) 353.
[12] I.H. Son, J. Hwan Park, S. Kwon, S. Park, M.H. Rümmeli, A. Bachmatiuk, H.J. Song, J. Ku, J.W. Choi, J.-M. Choi, S.-G. Doo, H. Chang, Nat. Commun. 6 (2015) 7393.
[13] J.-G. Ren, Q.-H. Wu, G. Hong, W.-J. Zhang, H. Wu, K. Amine, J. Yang, S.-T. Lee, Energy Technol. 1 (2013) 77.
[14] L. Ji, H. Zheng, A. Ismach, Z. Tan, S. Xun, E. Lin, V. Battaglia, V. Srinivasan, Y. Zhang, Nano Energy 1 (2012) 164.
[15] H. Wu, G. Yu, L. Pan, N. Liu, M.T. McDowell, Z. Bao, Y. Cui, Nat. Commun. 4 (2013) 1943.
[16] C. Wang, H. Wu, Z. Chen, M.T. McDowell, Y. Cui, Z. Bao, Nat. Chem. 5 (2013) 1042.
[17] M.T. McDowell, I. Ryu, S.W. Lee, C. Wang, W.D. Nix, Y. Cui, Adv. Mater 24 (2012) 6034.
[18] M. Gu, Y. Li, X. Li, S. Hu, X. Zhang, W. Xu, S. Thevuthasan, D.R. Baer, J.-G. Zhang, J. Liu, C. Wang, ACS Nano 6 (2012) 8439.
[19] M.T. McDowell, S.W. Lee, J.T. Harris, B.A. Korgel, C. Wang, W.D. Nix, Y. Cui, Nano Lett. 13 (2013) 758.
[20] X.H. Liu, F. Fan, H. Yang, S. Zhang, J.Y. Huang, T. Zhu, ACS Nano 7 (2013) 1495.
[21] C.R. Becker, K.E. Strawhecker, Q.P. McAllister, C.A. Lundgren, ACS Nano 7 (2013) 9173.
[22] L.Y. Beaulieu, T.D. Hatchard, A. Bonakdarpour, M.D. Fleischauer, J.R. Dahn, J. Electrochem. Soc. 150 (2003) A1457.
[23] L.Y. Beaulieu, K.W. Eberman, R.L. Turner, L.J. Krause, J.R. Dahn, Electrochem. Solid-State Lett. 4 (2001) A137.
[24] D.P. Finegan, E. Tudisco, M. Scheel, J.B. Robinson, O.O. Taiwo, D.S. Eastwood, P.D. Lee, M. Di Michiel, B. Bay, S.A. Hall, G. Hinds, D.J.L. Brett, P.R. Shearing, Adv. Sci. 3 (2015), 1500332(1−11).
[25] M. Ebner, F. Marone, M. Stampanoni, V. Wood, Science 342 (2013) 716.
[26] C. Villevieille, M. Ebner, J.L. Gómez-Cámer, F. Marone, P. Novák, V. Wood, Adv. Mater 27 (2015) 1676.
[27] D.S. Eastwood, V. Yufit, J. Gelb, A. Gu, R.S. Bradley, S.J. Harris, D.J.L. Brett, N.P. Brandon, P.D. Lee, P.J. Withers, P.R. Shearing, Adv. Energy Mater 4 (2014), 1300506(1−7).
[28] O.O. Taiwo, D.S. Eastwood, P.D. Lee, J.M. Paz-Garcia, S.A. Hall, D.J.L. Brett, P.R. Shearing, ECS Trans. 69 (2015) 81.
[29] D.P. Finegan, M. Scheel, J.B. Robinson, B. Tjaden, I. Hunt, T.J. Mason, J. Millichamp, M. Di Michiel, G.J. Offer, G. Hinds, D.J.L. Brett, P.R. Shearing, Nat. Commun. 6 (2015) 6924.
[30] J. Gonzalez, K. Sun, M. Huang, J. Lambros, S. Dillon, I. Chasiotis, J. Power Sources 269 (2014) 334.
[31] J.M. Paz-Garcia, O.O. Taiwo, E. Tudisco, D.P. Finegan, P.R. Shearing, D.J.L. Brett, S.A. Hall, J. Power Sources 320 (2016) 196.
[32] E. Maire, P.J. Withers, Int. Mater. Rev. 59 (2013) 1.
[33] M. Stampanoni, A. Groso, A. Isenegger, G. Mikuljan, Q. Chen, A. Bertrand, S. Henein, R. Betemps, U. Frommherz, P. Böhler, D. Meister, M. Lange, R. Abela, in: U. Bonse (Ed.), Proc. SPIE, 2006, 63180M−63180M−14.
[34] D. Paganin, S.C. Mayo, T.E. Gureyev, P.R. Miller, S.W. Wilkins, J. Microsc. 206 (2002) 33.
[35] F. Marone, M. Stampanoni, J. Synchrotron Radiat. 19 (2012) 1029.
[36] M.D. Abramoff, P.J. Magalhaes, S.J. Ram, Biophot. Int. 11 (2004) 36.
[37] W.E. Lorensen, H.E. Cline, SIGGRAPH Comput. Graph 21 (1987) 163.
[38] L. Gireaud, S. Grugeon, S. Laruelle, B. Yrieix, J.-M. Tarascon, Electrochem. Commun. 8 (2006) 1639.
[39] B. Key, R. Bhattacharyya, M. Morcrette, V. Seznéc, J.-M. Tarascon, C.P. Grey, J. Am, Chem. Soc. 131 (2009) 9239.
[40] M.J. Chon, V.A. Sethuraman, A. McCormick, V. Srinivasan, P.R. Guduru, Phys. Rev. Lett. 107 (2011), 045503(1−4).
[41] P. Limthongkul, Y.-I. Jang, N.J. Dudney, Y.-M. Chiang, Acta Mater 51 (2003) 1103.
[42] S.W. Lee, M.T. McDowell, J.W. Choi, Y. Cui, Nano Lett. 11 (2011) 3034.
[43] J.L. Goldman, B.R. Long, A.A. Gewirth, R.G. Nuzzo, Adv. Funct. Mater 21 (2011) 2412.
[44] X.H. Liu, J.W. Wang, S. Huang, F. Fan, X. Huang, Y. Liu, S. Krylyuk, J. Yoo, S.A. Dayeh, A. V Davydov, S.X. Mao, S.T. Picraux, S. Zhang, J. Li, T. Zhu, J.Y. Huang, Nat. Nanotechnol. 7 (2012) 749.
[45] M. Pharr, K. Zhao, X. Wang, Z. Suo, J.J. Vlassak, Nano Lett. 12 (2012) 5039.
[46] X.H. Liu, L. Zhong, S. Huang, S.X. Mao, T. Zhu, J.Y. Huang, ACS Nano 6 (2012) 1522.
[47] S. Huang, F. Fan, J. Li, S. Zhang, T. Zhu, Acta Mater 61 (2013) 4354.
[48] Y.S. Choi, M. Pharr, C.S. Kang, S.-B. Son, S.C. Kim, K.-B. Kim, H. Roh, S.-H. Lee, K.H. Oh, J.J. Vlassak, J. Power Sources 265 (2014) 160.
[49] I. Ryu, J.W. Choi, Y. Cui, W.D. Nix, J. Mech, Phys. Solids 59 (2011) 1717.
[50] Y. Li, K. Yan, H.-W. Lee, Z. Lu, N. Liu, Y. Cui, Nat. Energy 1 (2016), 15029(1−8).